SAND2011-3708C

Proceedings of the ASME 2011 5th International Conference on Energy Sustainability & 9th Fuel Cell Science,
Engineering and Technology Conference
ESFuelCell2011
August 7-10, 2011, Washington DC, USA

ESFuelCell2011-54216

Modeling and Validation of Heliostat Deformation Due to Static Loading

Adam C. Moya, Clifford K. Ho

Concentrating Solar Technologies Department, Sandia National Laboratories, P.O. Box, 5800,
Albuquerque, NM 87185-1127, USA, (505) 284-5010, acmoya@sandia.gov

Abstract

Accurate and reliable models are necessary to predict the performance and efficiencies of concentrating solar power plant components and systems such as heliostats and central receiver systems. Heliostat performance is impacted from effects such as wind and gravity, and understanding the impact of these loads on the optical performance can yield heliostat designs that are potentially cheaper, while maintaining required structural stability. Finite element models of heliostats at the National Solar Thermal Test Facility (NSTTF) at Sandia National Laboratories in Albuquerque, NM, were developed to simulate displacements under different loading scenarios. Solidworks was used to develop the three-dimensional model of the NSTTF heliostat, and Solidworks Simulation was used to perform the finite element analysis with simulated loads along different points of the heliostat. Static displacement tests were performed on the NSTTF heliostat in order to validate these FEA models. The static test results provide us with a data set in which to properly calibrate the FEA model to better represent the NSTTF heliostat for future simulations of optical performance with impacts of wind and gravity sag.

In addition to a single model validation, this real world test provides a method to validate and understand the structural stability of a heliostat under static loads.

Introduction

The need to reduce the costs of heliostats is important to reduce the levelized cost of electricity. The ability to predict deformations in the heliostat due to wind and gravity loading can be very beneficial to improve designs and reduce costs of manufacturing by preventing over designing and reducing test time. An accurate finite element model becomes a very valuable asset as heliostat construction generally consists of approximately 50% of the total cost of a power tower project [1].

A 3D CAD assembly was made of the NSTTF heliostat using Solidworks and Solidworks Simulation 2010 to demonstrate this modeling capability. Using the finite element code coupled with Solidworks Simulation 2010 and real world test results, the model was verified with regards to static displacement events such as gravity. With respect to dynamic loads such as wind, a modal analysis and test was conducted on the same heliostat as presented in a companion paper [2].

Heliostats have been studied in the past for methods to improve design and reduce cost, and very little has been published regarding full-scale validation and testing. L.M. Murphy et al. studied structural design improvements in stretched membrane heliostats due to natural phenomena and the resulting impact on cost and performance [3]. In contrast, this paper seeks to provide an inexpensive method to perform and validate such studies. Others have also presented papers researching wind load effects and mitigation for heliostats [4-5]. Another similar study performed at Sandia National Laboratories looks at gravity effects on concentrating solar collectors. This mostly pertained to finite element methods for modeling solar troughs and provides no test validation [6]. This paper focuses on the development of a finite element model of a heliostat at the National Solar Thermal Test Facility at Sandia National Laboratories in Albuquerque, NM, and a full-scale test validation through static loading

CAD Model

A Solidworks model of the NSTTF heliostat was developed using a top down approach [7]. This top down methodology allows for the user to easily change the configuration of the heliostat without the need to modify any individual components. The NSTTF Heliostat consists of 25 facets that are individually canted and focused based on heliostat location with respect to the tower. Using reference geometry and a design table in Solidworks, the model allows the user to change three important parameters, the Elevation, the Azimuth, and the focal length of the mirrors. Once these parameters are changed, the model will rebuild to the new desired configuration. The CAD model is used in other codes such as computational fluid dynamics and ray tracing, which have specific coordinate systems. Being able to change the azimuth angle relative to a common coordinate system in Solidworks makes it more convenient to model the system in other software codes.

Figure 1: Top Down CAD Model of NSTTF Heliostat

Shown in Fig. 1 is the NSTTF Heliostat model at a 45 degree orientation with the mirrors focused on a target located 100 meters away. Each facet has 3 adjustment points that control the canting of the mirrors, while there is one central bolt that is used to focus the mirrors by pulling the mirror into a concave shape. To achieve this effect in the model, each mirror is curved based on the radius required for a particular focal length given in the design table. The design table is a feature in Solidworks that lets the user change certain dimensions or relations in a model or assembly simply changing a value in an Excel spreadsheet.

For FEA purposes, the model was constrained at the base of the Heliostat underneath the azimuth motor. For static simulations, the azimuth motor was assumed to be a rigid body constrained to the yoke tubes. We do not believe that the vertical loads in this study will cause a significant amount of motion in the azimuth drive. The simulations that were conducted consist of gravity and point loads that were strategically placed on individual trusses. Each of these point loads was replicated during the static load testing phase of the project to validate the model.

FEA Model

An adaptive mesh had to be used in order to capture all components from the large yoke tubes to the small adjustment bolts. A global mesh size of 28.32 mm was used which resulted in over 1,800,000 elements and an average computation time of more than 20 hours. A grid convergence study was performed to ensure the mesh was sufficiently refined. Different meshing techniques using shell and beam elements was explored and abandoned due to modeling complications. These complications include complex geometry and sharp corners of the beam elements, i.e., the trusses. Also adding to the complexity was the curved nature of the mirrors, and special contact conditions between the mirror facets and the bolts that constrain them.

If these complications can be addressed in the future, simulation time can easily be reduced. In addition to the fine mesh size, certain contact conditions needed to be included for the geometry of the canted facets.

The first simulation evaluated the effects of gravity on the heliostat in the horizontal configuration. The resulting displacement due to gravity gives us a baseline condition of the heliostat prior to any point loads being applied, and thus one can obtain a relative displacement from the model that is comparable with that from static load testing. This gravity study resulted in a maximum displacement of 5.6 mm along one of the center trusses, mostly due to bending in the torque tube. A displacement plot of this gravity simulation is shown in Fig. 2.

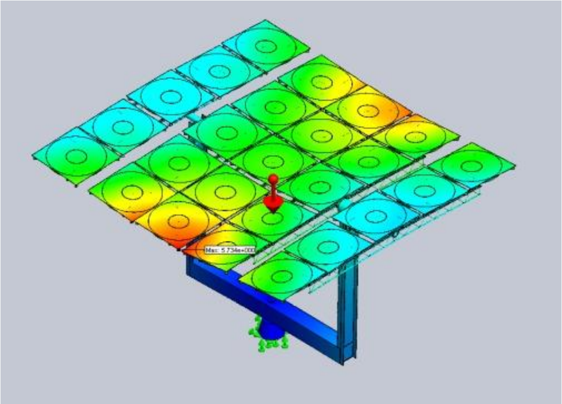

Figure 2: Gravity Deformed Heliostat in Horizontal Orientation

1. Static Displacement Testing

A test was performed to determine experimental displacements under static loads to verify the displacements predicted by the model. This test consisted of hanging free weights from selected points while recording displacements before and after. Three different methods for measuring displacements were deployed to determine the most accurate and efficient method for this type of model validation. The test apparatus is shown in Fig. 3 with measurement and load locations clearly labeled. The three individual measurement locations also represent a different measurement device or method. L1 and L2 correspond to the different load locations marked by the red arrows. These loads were applied by attaching a chain to the corresponding truss member and suspending previously measured weights. M1 corresponds to the location where the vertical ruler displacements were taken. M2 corresponds to the location were the string potentiometer was attached and M3 is the measurement location for the Leica Disto-Meter. These methods are further explained below.

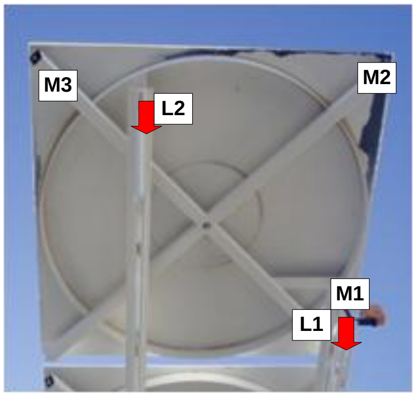

Figure 3: Test Apparatus and Measurement Locations

The first measurement method uses an automatically leveling laser that is attached magnetically to the facet at location M1. This level displayed a laser line on a ruler that was mounted vertically nearby. Since the laser automatically levels within a given range, a displacement can be obtained simply by reading the scale before and after loads are applied. The laser ruler displacement method can be estimated to have a minimum uncertainty of plus or minus 1 mm due to laser width and ruler tics. User error and wind excitation of laser will also add to this uncertainty. An image of this method is shown in Fig 4.

Figure 4: Ruler Displacement Method

The second method used a laser distance meter that is produced commercially for construction and survey use. The Leica Disto D8 model has a stated accuracy of plus or minus 1 mm with a range up to 200 meters. This method proved to be the easiest one to deploy. The meter simply needed to be mounted on a tripod, and leveled appropriately. This device is shown in Fig.5.

Figure 5: Leica Distance Meter

The third and final method utilizes a device called a linear position transducer or a "string potentiometer". This device outputs a voltage from a potentiometric voltage divider circuit as a string is pulled out from its coil. A displacement can be found by recording two voltages from this potentiometer when the string is pulled. A linear fit equation from previously calibrated data is used to obtain a displacement based from the two recorded voltages. This calibration resulted in an accuracy of plus or minus 0.13 mm and thus this method is the most accurate method used in this test. The calibration of this device consisted of systematically “pulling” the string while recording displacements off of a scale and the corresponding voltage. This calibration was done twice; once with a constant input voltage via a DC power supply, and once from a 9 volt battery. Both results were similar. A photo of the string potentiometer and the calibration data are shown Fig. 6 and Fig. 7 respectively.

Figure 6: String Potentiometer Used in Displacement Testing

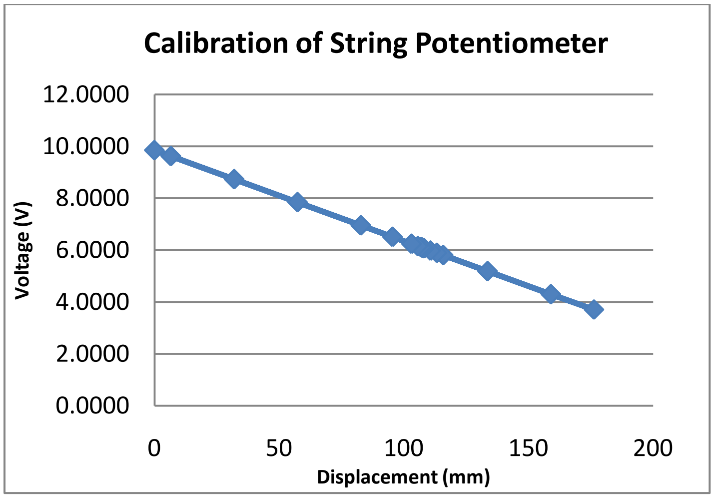

Figure 7: Calibration Data of String Potentiometer

The static load test scenario consisted of suspending weights via a chain from an individual truss on the heliostat. The loads applied ranged from 0 to 75 lbs using Olympic weights and a standard chain. These loads were chosen to provide proof of a linear displacement while both maintaining a high factor of safety and providing a measurable displacement. The chain and hook assembly was weighed prior to the test at approximately 10 lbs. This mass was accounted for while performing the static load tests.

Displacements were recorded before and after suspending each weight at each location. The load was varied as to verify a linear displacement behavior as predicted. Seven displacements were recorded per location as shown in Fig. 9. This particular data set is the result of loads placed on the far end of the smaller truss on the far end of the heliostat. Note that the displacements at positions M1 and M2 are very close, while the displacements at M3 are less. These results demonstrate that the truss assembly is bending about two different axis and exhibiting some twisting behavior.

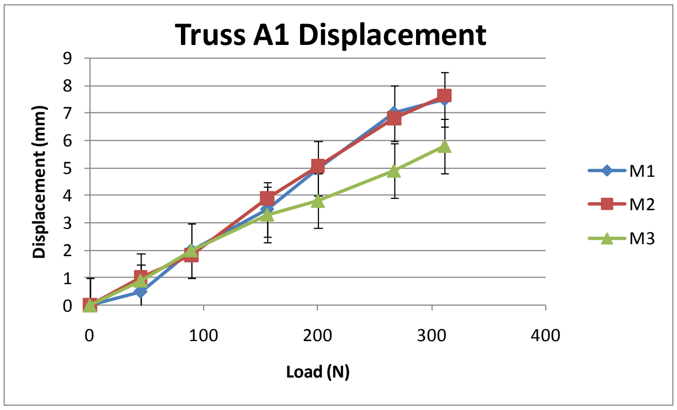

Figure 8: Experimental Displacement Results under Varied Loads on Far Truss

Data similar to Fig. 8 was recorded for 3 different truss assemblies, all of which demonstrate the same linear behavior.

Model Adjustments and FEA Results

Initially, the results from the static displacement test did not agree with the results from the Solidworks simulations. Discrepancies between the simulated and measured displacements were likely caused by inaccuracies in the material properties used in the model (e.g., modulus of elasticity) and possible backlash and slop in the gears, which was not initially modeled. To account for this, the models material properties were modified slightly and special contact conditions were used as to give us a well calibrated model.

The modulus of elasticity for the steel components was the only material property modified to allow the deformation in the model to match the test results. These material properties were changed by approximately 5.0% from the original

Solidworks values to better match the steel properties of A36 mild steel that was specified in the original heliostat construction plans. The final value used for Young's modulus was $1.9\ x\ 10^{11}\,\frac{N}{m^2}$

.

A special contact condition was applied to account for backlash or "gear slop" in the elevation motor. This contact condition simulated kinetic friction between the torque tube and the yoke supports. This parameter was a variable that was tuned to fit the test data similar to that of the modulus of elasticity and is defined by Solidworks as a value between 0 and 0.5 [8]. After several iterations, it was found that a friction coefficient of 0.2 was the most appropriate for simulating the backlash present in the system (see Appendix for friction study).

Fig. 9 is a displacement plot of the heliostat in the horizontal position that represents the static load test that was conducted. Fig. 10 and Fig. 11 show the improvement in accuracy that calibration of the Young's modulus and contact condition allowed. This data suggests that the FEA analysis was under predicting the displacements before calibration, and through proper calibration, the model can be improved. The calibration of the model is still being further refined to better match test results.

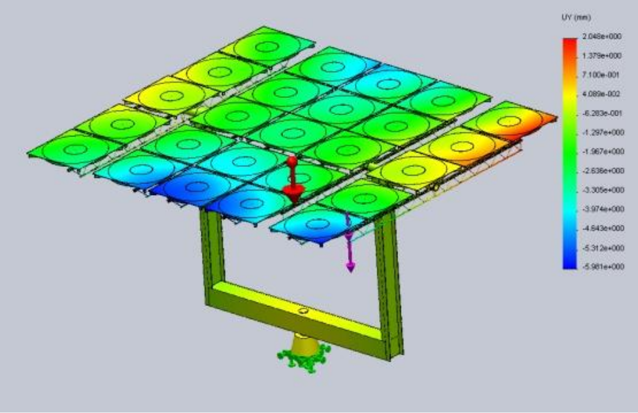

Figure 9: Displacement Plot of Heliostat Under 50lb Load at Position L1. Red Arrow Represents Gravity.

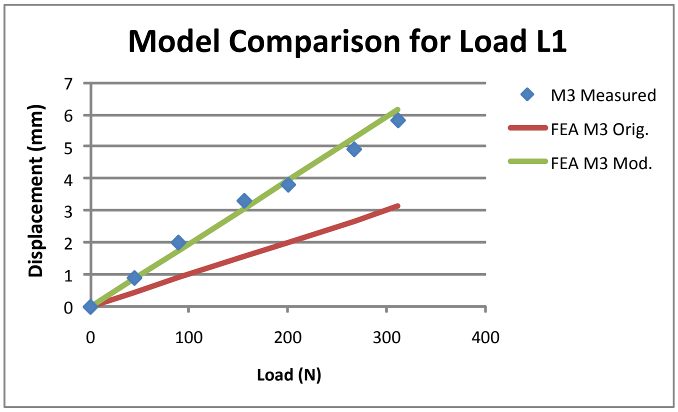

Figure 10: Displacement Predictions Before and After Model Calibration for Load L1 at Position M3

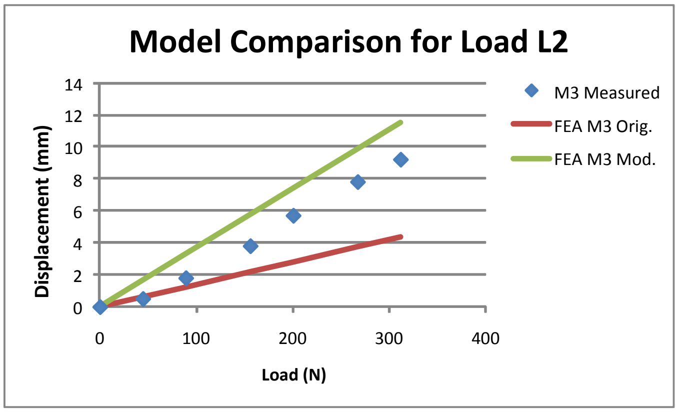

Figure 11: Displacement Predictions Before and After Model Calibration for Load L2 at Position M3

Measurement Uncertainty

Several sources of uncertainty may have affected the measurements. Based on experience (data recording, visual inspection, etc.) and experimental data, it is safe to assume wind had the largest effect on displacement measurement uncertainty. Windy conditions can cause an uncertainty in all three techniques. The wind causes the heliostat structure to vibrate, and also causes oscillation in the string used for the potentiometer. This has an extreme effect on the displacement reading in the string potentiometer due to its high sensitivity. It was very difficult to obtain accurate data during windy conditions. A small percentage of readings do show some error due to wind, and approximated average was taken at that time.

To determine the consistency of the measurement technique, the linear behavior of the displacement as shown in Fig. 10 is analyzed. By performing a least squares fit and averaging the coefficient of determination (R^2) for each loading scenario, the consistency of the measurements can be assessed. This R^2 value represents how well the linear regression fits the measured data, and thus how linear the displacement is. Since a linear behavior is expected in the elastic region of the structural deformation, the relative error in the data can be quantified through the coefficient of determination. Table 1 shows the averaged uncertainty percentages for each method which were acquired using equations 1-4 [10-11].

$$R^2 = 1 - \frac{SS_{err}}{SS_{tot}} \quad (1)$$

$$error\ \% = (1 - R^2) * 100 \quad (2)$$

$$SS_{tot} = \sum_i (y_i - \bar{y})^2,\ SS_{err} = \sum_i (y_i - f_i)^2 \quad (3\text{-}4)$$

Equation 1 is the definition for the coefficient of determination that is generally used for linear regression. The closer this value is to one, the better the linear regression fits the data. Equation 2 gives us an error percentage by which the linear regression is different from measured data. This is a quantitative measurement of how consistent the data set is in terms of linearity. Equations 3 and 4 are known as the total sum of squares and the residual sum of squares respectively. In these relationships; y_i is the recorded values from the data set, $\bar{y}$ is the mean of the recorded values, and f_i are the predicted values from the linear regression. As expected, the highest error is associated with the laser-ruler method at 2.04%. This method required a determination of the position of the laser light on the ruler, which was difficult to read.

Table 1: Measurement Uncertainty

Measurement Technique	**Error %**
String Potentiometer	1.01
Leica Disto-Meter	1.16
Laser – Ruler	2.04

Based on the results, the accuracy of any of the methods should suffice for static displacement testing, and the preferred method depends on user preference and ease of deployment. The least accurate as well as most difficult to use is the laser – ruler method. With a measurement uncertainty of 2.04% (table 1), the laser - ruler method is the least favorable for measuring deflections. The recommended measurement method is the Leica Disto D8 laser distance meter. This method is the easiest to deploy and has comparable results with the string potentiometer, which is the most sensitive and accurate method tested. However, rigorous calibration of the string potentiometer was required, and it was very sensitive to wind.

Future Work

The models developed in this study are being used to evaluate heliostat performance and impacts due to dynamic loads such as wind [2]. With dynamic simulation capabilities and field measurements, the vibration of a heliostat due to a wind load can be recorded and then replicated in Solidworks. This simulation will then give a maximum deformed shape for a given wind condition that can be used in an optical ray tracing code to determine beam quality degradation for a particular heliostat. This method of estimating efficiency loss due to wind excitation may eventually be applied to the entire NSTTF heliostat field in real time by instrumenting them with the appropriate accelerometers and monitoring equipment. One would then be able to see operating conditions in real time based on wind and acceleration data.

With respect to heliostats and other CSP applications, the most important parameter obtained through finite element analysis is displacement. Since displacement in the mirrors affects the accuracy of the reflected sunlight, additional studies are being performed to determine impacts of displacements on optical performance. For example, material properties such as the visco-elastic behavior of the mirrors and their adhesives can change due to time, temperature, and the elements [9]. This can cause some unexpected behavior with regard to heliostat optical performance, and models are needed to understand this behavior.

Conclusion

This paper describes the development of a heliostat finite-element model and full-scale testing using static loads for validation. During the test, several methods were evaluated to measure the displacements caused by static loads on different points on the heliostat. The best device for measuring displacements was found to be the Leica Disto 8 laser-distance meter. The Leica manufacture states and accuracy of plus or minus 1 mm when measuring distances, however, in the static load tests the results show that the meter was comparable to the string potentiometer which was accurate to within 0.13 mm. The Leica device was the easiest to deploy as it simply required leveling the tripod and placing a marker on the point of interest while recording displacements from the digital display. All measurements can be made at ground level, and are easily recorded either by hand or a Bluetooth enabled PC.

This paper provides a tested and verified tool for manufactures to validate FEA models of heliostats with regards to static loading. This is the first step in model validation prior to dynamic studies as presented in a companion paper. The results of the FEA model were able to replicate the general displacements and trends observed in the tests. With some slight modifications to the modulus of elasticity and contact conditions, the comparison between the Solidworks results and the test data were improved. Further optimization of material properties and contact conditions is ongoing to develop a fully calibrated model.

Acknowledgments

The authors would like to acknowledge test support from Todd Griffith (Sandia) and Patrick Hunter (Sandia) for contributing necessary equipment to conduct tests and performing necessary calibrations. The authors would also like to acknowledge Daniel Fisher (Sandia) for aid in the static load testing and Joshua Christian (Sandia) for aid with CAD modeling.

Sandia National Laboratories is a multi-program laboratory managed and operated by Sandia Corporation, a wholly owned subsidiary of Lockheed Martin Corporation, for the U.S. Department of Energy's National Nuclear Security Administration under contract DE-AC04-94AL85000.

Nomenclature

CSP – Concentrated Solar Power
FEA – Finite Element Analysis
Laser – Leica Disto™ D8 laser distance meter
NSTTF – National Solar Thermal Test Facility, SNL
SP – String Potentiometer
T – Internal Torque applied to torque tube during static testing
J – Polar Moment of Inertia
c = Outer radius of shaft
dA = Area of element located at ρ
L = Entire length of shaft
W = Weight of assembly
G – Shear Modulus of Elasticity
Φ – Angle of twist
δ - Deflection
μ - friction coefficient used in simulation

2. References

[1] Zang, Chuncheng; Wang, Zhifeng; Wang, Yahzhong; Liu, Xiaobing; Zhang, Xiliang (2010). Structural Design and Analysis of the Toroidal Heliostat. ASME Journal of Solar Energy Engineering, November 2010, Vol. 132/041007-1

[2] D. Todd Griffith, Adam C. Moya, Clifford K. Ho, and Patrick S Hunter, (2011). Structural Dynamics Testing and Analysis for Design Evaluation and Monitoring of Heliostats. *Proceedings of the ASME 2011 5th International Conference on Energy Sustainability & 9th Fuel Cell Science, August 7-10, 2011, Washington DC, USA*

[3] L.M. Murphy, D. Simms, D.V. Sallis (1986). Structural Design Considerations for Stretched-Membrane Heliostat Reflector Modules with Stability and Initial Imperfection Considerations. Solar Energy Research Institute, SERI/TR-253-2338

[4] J.A. Peterka, N. Hosoya, B. Bienkiewicz, J.E. Cermak (1986). Wind Load Reduction for Heliostats. SERI and Colorado State University

[5] Zhifeng Wang, Zhiyong Wu, Xiaobin Liu, Zhengnong Li. Wind Dynamics Testing on Dohan Heliostat. *Proceedings of ISES Solar World Congress 2007: Solar Energy and Human Settlement*

[6] Christian, J.M., Ho, C.K., "Finite Element Modeling of Concentrating Solar Collectors for Evaluation of Gravity Loads, Bending, and Optical Characterization," *Proceedings of the 4th International Conference on Energy Sustainability*, May 17-22, 2010, Phoenix, Arizona, USA, ES2010-90050

[7] Sciortino, A. (2005, Aug/Sep). Take it from the top. CAD User Mechanical Magazine, 18 (8). *http://www.caduser.com/reviews/reviews_print.asp?a_id=247*

[8] Solidworks Simulation Online Help Files, *http://help.solidworks.com/2010/english/SolidWorks/cworks/LegacyHelp/Simulation/Dialog_Box_Help/ID_HELP_WELDS_CONTACT.html*

[9] Henry H. Fong, (1978). Lessons Learned from My Early FEA Career, 1.C Structural Analysis of Solar Energy Heliostats. Department of Energy / Southern California Edison 10-MW Solar One Pilot Plant, Daggett, California, *http://www.feapublications.com/news_2008/HFong_1C.pdf*

[10] Draper, N.R. and Smith, H. (1998). *Applied Regression Analysis*. Wiley-Interscience.

[11] Everitt, B.S. (2002). *Cambridge Dictionary of Statistics* (2nd Edition)

[12] R.C. Hibbeler (2008). Mechanics of Materials 7th ed. Pearson Prentice Hall

Appendix

Friction Study

The idea to use friction as a replacement for the additional displacement due to "gear slop" had to first be explored as to ensure this was an accurate assumption. This additional friction constant was only applied between two concentric cylinders on the surfaces where the torque tube meets the yoke members. Initially the load on each side of this fulcrum was equal due to gravity, yet once the static test loads were applied, there exists a different case. The load was now uneven, thus there exists a moment applied on the torque tube. This is illustrated in Fig. 12.

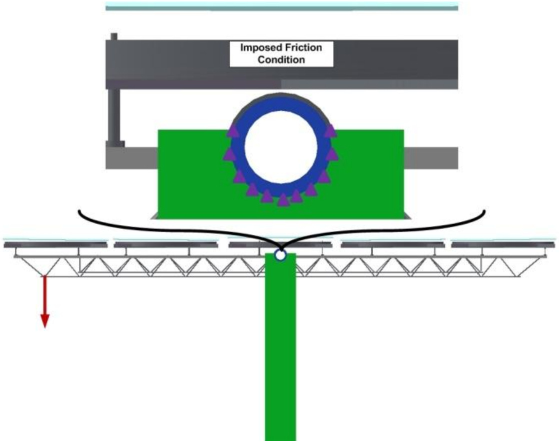

Figure 12: Friction Condition Applied to Torque Tube

This moment causes the torque tube to twist within the gear casing in the elevation motor until the gears contact. Since the CAD model is not this detailed, one method to simulate this twisting behavior was to modify the friction condition between the torque tube and its supports. This method assumes that the angle of twist due to the torsional loading will in turn simulate an additional displacement. This is explained in the equations 5 through 8. A derivation of equation 8 can be found in the appendix [12]

$$T = \frac{\tau_{max}}{c}\int_A \rho^2 dA \quad (5)$$

The internal torque at any point within the shaft is a function of ρ, the distance from the center of the shaft. The maximum shear stress, τ_{max}, is calculated by finite element method in Solidworks Simulation (5).

$$\Phi = \int_0^L \frac{T(x)dx}{J(x)G} \quad (6)$$

$$\delta = l\sin(\Phi) + l\sin(\Phi_{friction}) \quad (7)$$

$$\Phi_{friction} = f(\mu, T, W) \quad (8)$$

The angle of twist imposed on the torque tube is also dependent on the face on which it rests. If it is assumed that the two concentric cylinders are free to rotate, then the only force resisting the torque is that of friction. This implies there is an additional displacement due to the twist allowed between concentric faces. Here the angle of twist due to friction is defined as a function of the internal torque, the coefficient of friction, and the weight of the assembly. This method seems to work well as a simulation tool and allows us to simulate backlash. Figure 13 shows the contributions of displacements caused by the normal angle of twist (Φ) and the gear backlash or slop, which is represented by an additional frictional angle of twist ($\Phi_{friction}$) allowed in the simulation. At some point in the loading, the contribution from gear backlash will be maximized and any additional displacement will be caused by elastic deformation. Therefore, the use of a friction condition to represent gear backlash may not be valid at higher loads. This is demonstrated in Fig. 13.

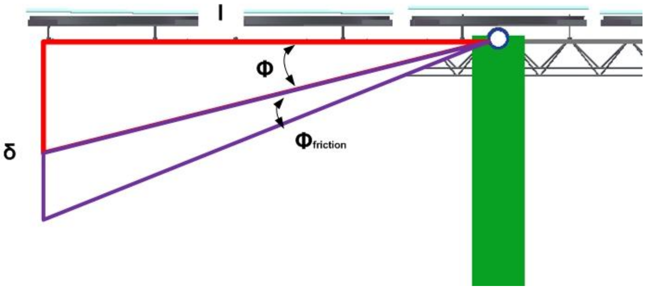

Figure 13: Angle of Twist Additive Behavior (Exaggerated)

Multiple studies were run to determine the effect friction would have on the model. Figure 14 shows this friction study by comparing displacement vs. friction coefficient. To achieve these friction results, the same simulation was run using different friction coefficients to obtain a displacement near that of the measured results for a given load. This is simply programmatically adjusting the friction coefficient until the results match reality.

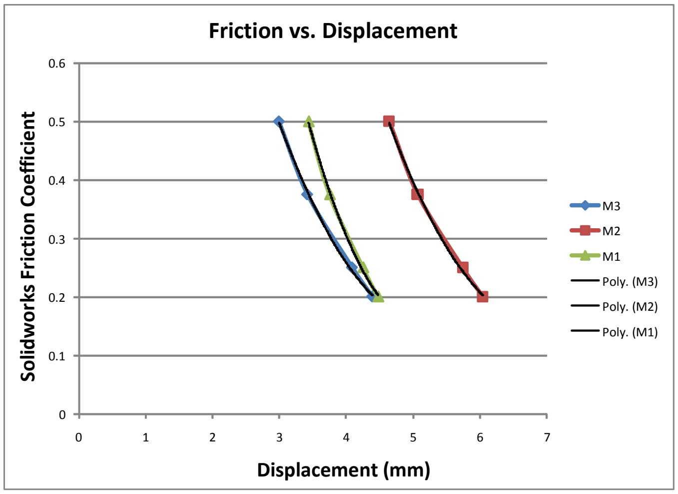

Figure 14: Friction Coefficient vs. Displacement for a 50lb Load

The assumption is that friction would simply cause an offset in the displacements, and one would be able to scale the results to match the test measurements. Fig 14 demonstrates the effect friction has on the models predicted displacements. As Fig 14 displays, the deflection increases as the friction coefficient decreases. The comparison of these results to the original data shows that this particular friction addition did add a constant offset as predicted in equation 3, and one can use this method as a simulation simplification to increase deflection.

Equation 8 Derivation

Given the general relation between the kinetic coefficient of friction and the force exerted due to friction, we can establish a general relationship for the total angle of twist. This is represented in the following derivation.

$$F_k = \mu_k F_n \ (9)$$

Equation 9 represents the resistive force due to friction. This relationship can then be utilized in the equations below to represent the shear stress due to friction (10) and the total internal torque due to friction and the applied load (12).

$$\tau = \frac{V}{A}, \tau_{friction} = \frac{\mu_k F_n}{A} \ (10)$$

$$T = \frac{\tau_{max}}{c} \int_A \rho^2 dA \ (11)$$

$$T_{total} = \frac{\tau_{\max} + \frac{\mu_k F_n}{A}}{c} \int_A \rho^2 dA \ (12)$$

Using the relationship described in equation 12, we can now come to a general relation for the total angle of twist due to the previously applied load and the new friction coefficient as shown in equation 14. Note that this equation does not represent any elastic deformation and is purely a representation of the angle of twist due to the imposed torque.

$$\Phi_{total} = \int_0^L \frac{T_{tot}(x)}{J(x)G} \ (13)$$

$$\Phi_{total} = \int_0^L \{ (\frac{\tau_{max}}{cJ(x)G} + \frac{\mu_k F_k}{AcJ(x)G}) \int_A \rho^2 dA \} \ (14)$$